Lasers in Surgery and Medicine 19:388–396 (1996)

Measurement and Modeling of Thermal Transients During Er:YAG Laser Irradiation of Vitreous

Jeffrey W. Berger, MD, PhD, Thomas W. Bochow, MD, Jonathan H. Talamo, MD, and Donald J. D'Amico, MD

Laser Research Laboratory, Department of Ophthalmology, Massachusetts Eye and Ear Infirmary, Harvard Medical School, Boston, Massachusetts 02114

Background and Objective: **We investigated the transient thermal behavior of vitreous in order to understand the local thermal effects of laser output, and to predict the potential for unintentional injury during Er:YAG laser vitreoretinal surgery.**
Study Design/Materials and Methods: **The output of a free-running Er:YAG laser (2.94 μm, 300 μs FWHM) was delivered through a fiberoptic and applied to en bloc samples of bovine vitreous. Temperature was measured with ultrafine thermocouples.**
Results: **For 6 mJ pulse energy at 10 Hz, a temperature rise of 20°C is measured 500 μm from the laser tip. The temperature rise is localized with a rapid fall-off greater than 1 mm from the energy source. At constant time-averaged laser power, the temperature profile is independent of repetition rate. Our finite-difference model generates results qualitatively consistent with measured data and allows for investigation of the influence of thermophysical parameters on heat transfer.**
Conclusion: **Thermal injury to ocular structures should be limited during intravitreal application of Er:YAG laser energy.**

Key words: erbium, heat transfer, infrared, modeling, vitreous

INTRODUCTION

Er:YAG laser radiation at 2.94 μm is strongly absorbed by tissue water, resulting in a very short optical penetration depth. For pure water, the absorption coefficient is 13,000 cm^{-1}, yielding a 1/e penetration depth on the order of 1 μm. Hence, the Er:YAG laser presents theoretical advantages for highly precise tissue removal.

Previous studies have explored the interactions of Er:YAG laser output with ocular tissues [1–9], and significant strides have been made toward incorporating the Er:YAG laser as a clinical tool for both anterior segment [8,10,11] and posterior segment ophthalmic applications [7,12]. While there have been extensive basic and clinical studies of CO_2 laser application in the vitreous [13–16], investigation of vitreoretinal applications for the Er:YAG laser are promising, yet limited [6,7,12,17,18].

To determine potential clinical utility, it is necessary to demonstrate efficacy and safety. Since the principal laser–tissue interaction following absorption of 2.94-μm radiation is heating of tissue, local temperature profiles need be investigated to understand and predict tissue changes adjacent to the energy source. Further, temperature measurements remote from the energy source are necessary to exclude the potential for untoward thermal injury to ocular structures. Finally, tissue ablation proceeds through photovaporization, hence the potential exists for injury

Accepted for publication November 9, 1995.

Address reprint requests to Jeffrey W. Berger, M.D., Ph.D., Retina Service, Department of Ophthalmology, Scheie Eye Institute, 51 North 39th Street, Philadelphia, PA 19104.

Presented in part at the 1995 meeting of the American Society for Laser Medicine and Surgery, San Diego, CA.

resulting from the acousto-mechanical sequelae of expansion and collapse of the vapor bubble [18].

In this report, we present measurements of intravitreal temperature measurements following application of Er:YAG laser energy and derive a simple model for predicting intravitreal transient thermal phenomena.

MATERIALS AND METHODS

Experimental Studies

A Coherent (Palo Alto, CA) Optima VTE Er:YAG laser delivered 300-μs pulses (full width, half-maximum) to a high mid-infrared transmitting fiberoptic. The fiberoptic was coupled to a custom-made handpiece with a fine quartz tip. Tip diameters ranging from 75–600 μm are available in our system, but in these studies, only the 200-μm-diameter tip was used. The pulse energy was varied between 2 and 20 mJ per pulse, and the laser was operated at 5–10 Hz. The laser was checked for calibration prior to and following each experiment with a DigRad R752 Universal Radiometer (Oriskany, NY).

Bovine eyes were obtained from a local abattoir and were used promptly. The eye was opened with a razor blade in the equatorial plane, and the intraocular contents was expressed en bloc. The lens and adherent uveal tissue were removed with sharp dissection, leaving approximately 5–10 ml of vitreous. The vitreous was then placed in a shallow, insulated styrofoam cup for temperature measurements. Experimental studies were performed at room temperature.

Temperature measurements were performed with a personal-computer–based data-acquisition system (Fig. 1). Up to three HYP-0, modified hypodermic needle, 33-gauge copper-constantan T-type thermocouples (Omega Corporation, Stamford, CT) were inserted into each sample. The thermocouples were connected to a terminal board with an isothermal plate and subsequently to a 12-bit resolution analog-to-digital converter (WB-FAI-B8, Omega). The digital output was sampled by an IBM personal computer with QuickLog software (Omega). The implicit properties of the thermocouples combined with the resolving power of the analog-to-digital conversion yields a resolution of 0.3°C and an accuracy of ± 1.5°C. The response time of the system is on the order of 0.1–0.3 s.

Modeling Studies

Heat transfer in the vitreous was modeled following the general approach described by La-

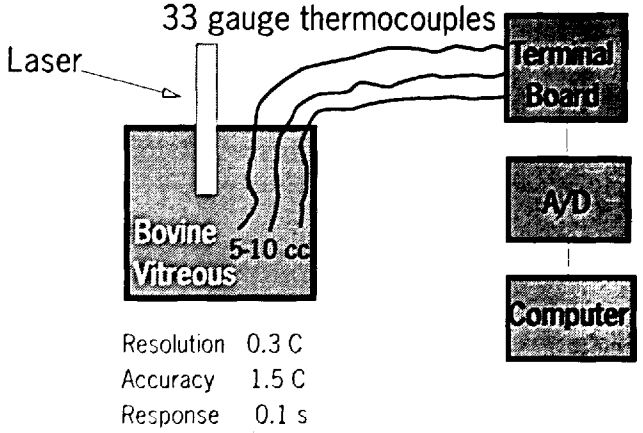

Fig. 1. Experimental configuration for measurement of thermal transients in vitreous. The output of a free-running Er:YAG laser was directed into a styrofoam cup containing 5–10 cc of excised, en bloc bovine vitreous. The laser output at 2.94 μm was coupled to a fiberoptic and custom-made handpiece, with final delivery through a 200-μm quartz tip. Temperature was measured with 33-gauge copper-constantan thermocouples. The signal was calibrated and digitized and sent to a personal computer for storage and analysis.

gendijk [19]. For simplicity, the vitreous is idealized as a sphere of radius R, with the energy source positioned at the center of the sphere. The sphere is then discretized into N spherical shells, and the heat transfer between the shells is calculated (Fig. 2).

The flow of heat is calculated through the iterative application of Fourier's law. This relation for heat transport states that the total thermal energy (Q) conducted into a volume is proportional to the temperature difference across the volume (ΔT), the area over which it is conducted (A), the time available for transport (Δt), and is inversely proportional to the length (ΔL) over which it is conducted,

$$Q = k\,\Delta T\,A\,\Delta t/\Delta L \qquad (1)$$

where k is the proportionality constant, and is referred to as the thermal conductivity [19].

The geometry is depicted in Figure 2, and the energy balance equation for the ith node is described by

$$K_{i,i-1}(T_{i-1}-T_i) + K_{i,i+1}(T_{i+1}-T_i) + H\,\Delta V_i = \rho\Delta V_i C_p(T'_i-T_i)/\Delta t \qquad (2)$$

where T_i and T'_i are the temperatures of the ith node at times t and $t+\Delta t$, K_{ij} is the thermal conductance between the ith and jth nodes and is

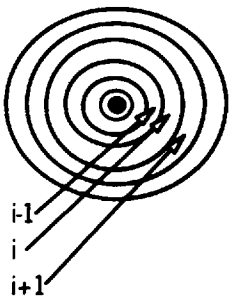

Typical Parameters

Spatial discretization	200 um
Temporal discretization	100 ms
R = 5 mm	
C = 4 J/g-C	
k = 0.006 W/cm-C	
h = 0.006 W/cm^2 -C	

Fig. 2. Geometry of the heat transfer model. The energy is applied only to the innermost node, and heat transfer between neighboring nodes proceeds iteratively through application of Fourier's law. The energy balance equation for the *i*th node is described by $K_{i,i-1}(T_{i-1}-T_i) + K_{i,i+1}(T_{i+1}-T_i) + H\,\Delta V_i = \rho\,\Delta V_i\,C_p\,(T'_i-T_i)/\Delta t$ where T_i and T'_i are the temperatures of the *i*th node at times t and $t+\Delta t$, K_{ij} is the thermal conductance between the *i*th and *j*th nodes and is equal to kA/d where A and d are the area of contact and the linear separation between the nodes, ΔV_i is the volume of the *i*th node, H is the absorbed power in W/cm^3, ρ is the density of the material, and C_p is the specific heat of the material. The innermost node is spherical, while the remaining nodes are spherical shells. The nodes are uniformly spaced. Heat transfer among the *N* nodes is calculated, and a heat transfer term from the outermost shell to the environment is included.

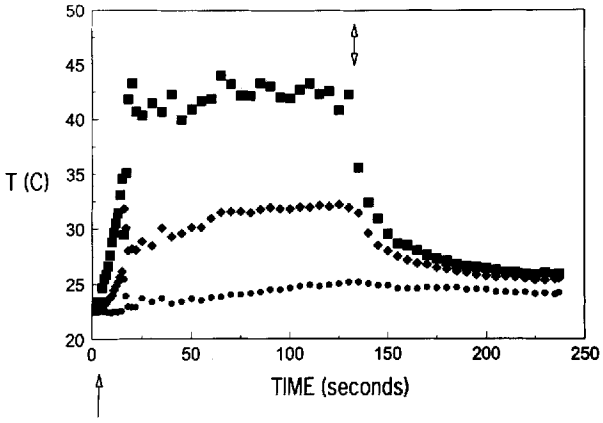

Fig. 3. Experimental measurement of thermal transients in bovine vitreous. The temperature of bovine vitreous is depicted at 0.5 (squares), 2.5 (diamonds), and 6 mm (circles) from the laser tip. The laser is turned on (arrow) and off (double-headed arrow) at 3 and 125 s, respectively. Here, 6 mJ was applied through a 200-μm tip at 10 Hz to ~5 ml of bovine vitreous.

equal to kA/d where A and d are the area of contact and the linear separation between the nodes, ΔV_i is the volume of the *i*th node, H is the absorbed power in W/cm^3, ρ is the density of the material, and C_p is the specific heat of the material.

At the surface, heat is allowed to flow toward the inner nodes. In addition, heat transfer from the material to the surrounding medium is described by a heat transfer coefficient, *h*, where the thermal conductance between the outer boundary and the environment is given by

$$K_{N,out} = h\,A. \qquad (3)$$

The ambient temperature is arbitrarily set to T = 0. The source term is specified to act only over the innermost node in the simulations described here, but in general, the geometry of the source term can be defined explicitly.

The spatial discretization and temporal discretization were 200 μm and 100 ms, respectively. For most calculations, the vitreous sphere was assumed to be 10 mm in diameter. Thermal tissue properties were derived from the literature. In accordance with previous studies, the heat capacity, thermal conductivity, density, and heat transfer coefficient are specified as C_p = 4 J/g-C, k = 0.006 W/cm-C, ρ = 1 g/cm^3, and h = 0.006 W/cm^2-C [19,21–23]. For 1,200 temporal iterations with a spatial discretization of 200 μm, ~20 min of computation time on an IBM 386 is required.

RESULTS

Experimental Studies

Representative thermal transient profiles for Er:YAG laser heating of bovine vitreous are depicted in Figure 3. The temperature rise following application of laser energy is biphasic with a rapid rise over 10–20 s, followed by a slower rise to a plateau with a time constant on the order of 50 s. For 6 mJ application, the time to achieve half of the total temperature rise is 10 and 12 s for measurements 0.5 and 2.5 mm from the laser source, respectively. When the laser is turned off, the sample temperature decreases in a similarly multiexponential fashion, falling to half of the maximum temperature at 6 and 12 s, for measurements 0.5 and 2.5 mm from the laser source, respectively.

The temperature rise was found to be a function of the laser power, but independent of the repetition rate with the power held constant. An example is depicted in Figure 4. With the power held constant at 60 mW, the temperature profiles for repetition rates of 5 (12 mJ/pulse) and 10 Hz (6 mJ/pulse) measured 1 mm from the laser source

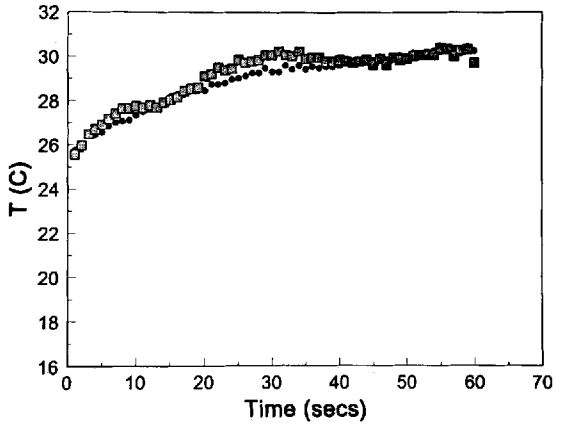

Fig. 4. The temperature rise in independent of repetition rate at constant power. The temperature rise of bovine vitreous is shown for 60 mW following irradiation at 5 Hz (12 mJ/pulse, squares) and 10 Hz (6 mJ/pulse, circles). The laser is turned on at time 0.

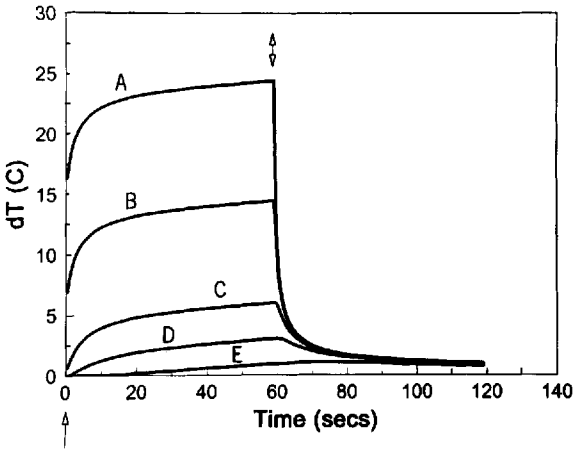

Fig. 5. Thermal transient curves generated by a finite-difference, heat transfer model for the temperature response of vitreous to Er:YAG laser irradiation. The laser is turned on and off at 0 (arrow) and 60 s (double-headed arrow), respectively. The vitreous is modeled as a sphere of radius 5 mm. Six millijoules at 10 Hz is applied to the innermost node. The temporal and spatial discretizations are 100 ms and 200 μm, respectively. The thermal conductivity and heat transfer coefficient are 0.006 W/cm-C and 0.002 W/cm^2-C, respectively. "Measurements" are made 0.4 (A), 0.6 (B), 1.2 (C), 2.0 (D), and 5 mm (E) from the energy source.

are nearly superimposable (and certainly within the measurement error).

Modeling Studies

Figure 5 depicts the change in temperature as a function of time, with temperature "measurements" performed at 0.4, 0.6, 1.2, 2.0, and 5.0 mm from the energy source. The laser is "turned on and off" at 0 and 60 s, respectively. A biphasic rise in the temperature is noted following application of energy. The temperature decay curve following the termination of irradiation is similarly biphasic. For measurement 0.6 and 2.0 mm from the energy source, the times to half-maximal temperature rise are 2 and 20 s, respectively. After the laser has been "turned off," the temperature falls to half of its maximum at 2 and 49 s, respectively.

The temperature rise as a function of laser energy following 10 s of laser irradiation is depicted in Figure 6. The thermocouple probe was positioned 1 mm from the laser probe tip. At higher energies, a nearly linear relation is observed. The temperature rise as a function of laser energy "measured" 1 mm from the laser source is also depicted in Figure 6. A strictly linear relation is predicted by the numerical model, and there is fair agreement between our model and experimental measurements.

The spatial profile of temperature is depicted in Figure 7 at 10, 60, 70, and 120 s following laser application. As previously, the laser is modeled to be "on" from 0 to 60 s. Notably, there is only small augmentation to the temperature at 60 s, when

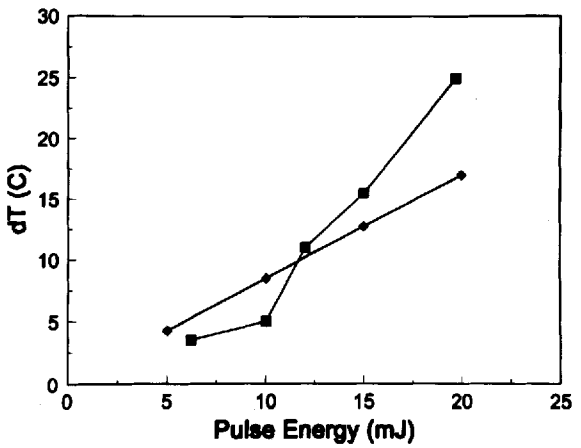

Fig. 6. A comparison of the measured (squares) and calculated (diamonds) temperature rise 1 mm from the laser source as a function of pulse energy. The experimental and modeling parameters are identical to those in Figures 3 and 5.

compared with the profile at 10 s. Further, there is rapid cooling during the first 10 s after the laser is turned off. Finally, the temperature rise is large near the energy source, but falls off rapidly at distances greater than 1 mm, falling to half-maximum in approximately 300 μm.

Several of the thermal parameters incorporated into the model were varied to investigate the potential contribution of these parameters to

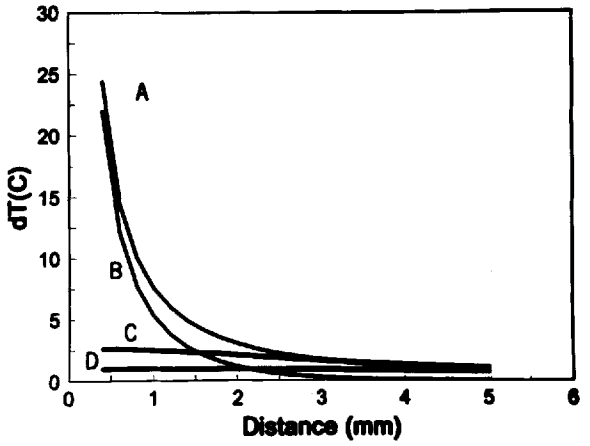

Fig. 7. Spatial temperature gradients generated by the heat transfer model. Laser parameters are identical with those described in Figure 5. The laser is "turned on and off" at 0 and 60 s, respectively. Temperature profiles are depicted as a function of distance from the energy source at 10 (B), 60 (A), 70 (C), and 120 seconds (D).

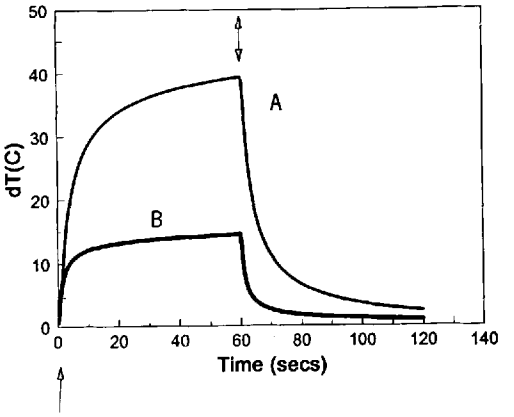

Fig. 8. Thermal transients generated by the heat transfer model. Measurements 600 μm from the energy source are depicted under conditions identical with those described in Figure 5. The laser is turned on and off at 0 (arrow) and 60 s (double-headed arrow), respectively. The simulations differ in the magnitude of the thermal conductivity. Thermal transients are depicted for thermal conductivities of 0.002 (A) and 0.006 (B) W/cm-C.

heat transfer phenomena. The heat transfer coefficient, h, was allowed to vary over the presumed physiologic range of 0.002–0.008 W/cm^2-C. The observed temperature profiles are essentially identical over this range. The size of the vitreous sphere was expanded to investigate the role of remote heat transfer phenomena on temperature in the vicinity of the laser source. For sphere diameters of 10–20 mm, the computed temperatures "measured" 400 μm to 4 mm from the laser source were essentially independent of the size of the spherical model.

The thermal conductivity, k, was varied, with the remaining modeling parameters held constant. The temperature rise near the laser source is depicted in Figures 8 and 9 for "measurement" 600 μm and 2.6 mm from the laser source, respectively. The maximum temperature is higher for lower values of the thermal conductivity (Figs. 8, 9). In addition, the kinetics of the temperature rise are somewhat slower for lower thermal conductivity. For k = 0.002 W/cm-C, the times to half-maximal temperature rise are 4 and 31 s for measurement at 0.6 and 2.6 mm, respectively. When energy deposition is stopped, the temperature drops to half-maximum value at 4 and greater than 60 s, respectively.

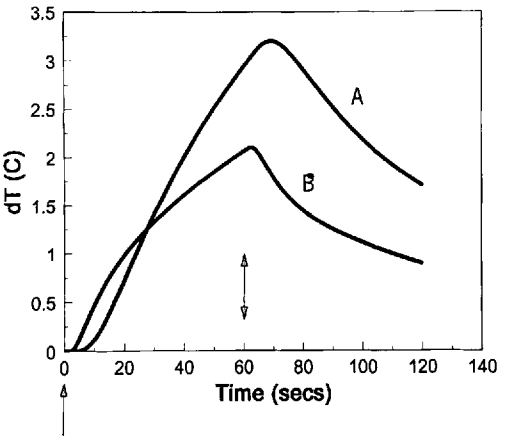

Fig. 9. Thermal transients generated by the heat transfer model. Measurements 2.6 mm from the energy source are depicted under conditions identical with those described in Figure 5. The laser is turned on and off at 0 (arrow) and 60 s (double-headed arrow), respectively. The simulations differ in the magnitude of the thermal conductivity. Thermal transients are depicted for thermal conductivities of 0.002 (A) and 0.006 (B) W/cm-C.

DISCUSSION

Several groups have investigated the use of infrared lasers for intravitreal applications [6,7, 12–18,24]. In many reports, the infrared laser serves to effectively transect experimental vitreous membranes, but damage to subjacent structures limited the applicability of this approach. The Er:YAG laser presents advantages over carbon dioxide and holmium sources. First, the absorption coefficient for tissue water at 2.94 μm is much higher, suggesting short optical penetra-

tion. Second, energy delivery is less cumbersome with Er:YAG when compared with the carbon dioxide laser.

Margolis et al. [6] employed a free-running Er:YAG laser with energies of 3–14 mJ/pulse to transect experimental vitreous membranes. At these energies, there was a greater likelihood of retinal injury when the laser tip was less than 2 mm from the retinal surface, although one membrane was successfully transected 800 μm from the retina without subjacent damage. Recently, Brazitikos et al. [12] demonstrated successful transection of 25 vitreous membranes at distances of 0.5–4.5 mm from the retinal surface in rabbit eyes. Non-hemorrhagic retinal damage was induced in one procedure. The pulse energies varied from 0.5 to 5.5 mJ. Whereas Margolis et al. employed a 200-μm tip, our system as described by Brazitikos et al. allowed for energy delivery to a tip diameter as low as 75 μm, yielding a higher radiant exposure (J/cm^2) for lower total pulse energy. Since tissue transection is a function of radiant exposure, but tissue damage from mechanical and thermal effects likely depends on the total deposited energy [18], smaller probe tips optimize the ablative capabilities with respect to the potential for untoward tissue injury. This report explores the diffusion of thermal energy from the target site and evaluates the potential for thermal injury to nearby structures.

Bende et al. measured thermal gradients in cornea following Er:YAG laser irradiation [5]. Using a 2-mm-diameter beam, with radiant exposure of 1.3–3 J/cm^2 and repetition rates of 1–4 Hz, the authors found a monotonic rise in corneal temperature over 100 s of irradiation, corneal cooling following cessation of irradiation with a drop to half-temperature at 19 s, and a nearly exponential fall in temperature with increasing distance from the source to half-temperature at 970 μm. The temperature increased linearly with repetition rate, but surprisingly, the temperature was independent of radiant exposure over 1.3–3 J/cm^2.

Our results are somewhat similar. In vitreous, there is a similar rise and fall in tissue temperature following application and cessation of laser energy; however, the thermal kinetics in vitreous are approximately two- to threefold faster (Fig. 3). This discrepancy may reflect differences in thermophysical properties or experimental technique.

In cornea, the temperature rise falls off sharply with increasing distance from the laser source [5]. We find similar results in vitreous (Fig. 3). In contrast, the temperature rise is independent of position over distances of 2–10 mm following Er:YAG irradiation of aqueous solution [8], possibly resulting from an acousto-mechanical mixing effect. Hence, the establishment of a temperature gradient depends sensitively on the mechanical properties of the medium.

It is intuitive to assume that the temperature rise depends on the total power delivered. For example, the temperature rise resulting from 2X joules delivered to a sample over 1 min should be greater than the temperature rise resulting from X joules. The data in Figures 4 and 6 support this notion. Alternately, Bende et al. report a temperature rise that does not change significantly when the pulse energy was varied by more than a factor of 2 at a constant repetition rate [5]. The physical explanation for this result is unclear.

Several models for heat transfer in ocular structures have been described [18,20,25,26] with most models capitalizing on the cylindrically symmetric ocular configuration. Since 1) there is rapid fall-off in temperature a short distance from the energy source, and 2) energy loss at the surface through radiation and convection are not likely to influence the local temperature rise near the energy source, we have idealized the experimental configuration with a spherically symmetric model. Our goal was not to construct a highly accurate, computationally demanding model, but to construct a simple model which would generate data qualitatively consistent with experimental measurements. The model is easily extended to an arbitrary geometry by modifying the nodal configuration and recalculating the thermal conductance value between each node. Our preliminary results in this area suggest that more complex models do not significantly alter the predicted transient thermal profiles. This notion is further supported by our results demonstrating that local temperature profiles are insensitive to boundary processes (i.e., the temperature near the laser source is independent of the surface heat transfer coefficient and the size of the vitreous sphere).

The insensitivity of the local temperature to remote effects is partial validation for our spherical model. In particular, we have modeled the laser energy to be imparted to the center of a sphere. However, we are more interested, for example, in the temperature at the retinal surface in the vicinity of an elevated vitreous membrane (Fig. 10). Since the local temperature depends on

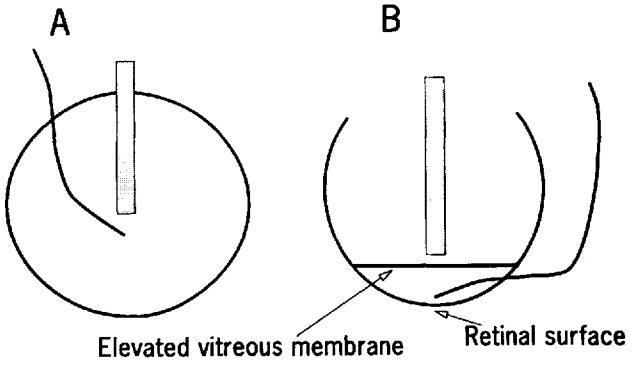

Fig. 10. Comparison of our spherical model for measurement and modeling of thermal transients in vitreous (A), with a geometry of clinical interest (B). In A, the laser delivers energy to the center of a sphere of vitreous. Panel B depicts transection of an elevated vitreous membrane located near the surface of the retina.

local conditions, but is not sensitive to remote effects, the *local* thermal response should be similar for both our model and geometries of clinical interest.

The laser wavelength is not explicitly specified in the model; however, two assumptions limit the applicability of the model. First, it is assumed that virtually all energy imparted to the sample is converted to thermal energy. We have verified this assumption for Er:YAG laser energy; the temperature rise of aqueous solution subjected to Er:YAG laser energy rises according to straightforward calorimetric predictions [8]. Second, it is assumed that all energy is deposited to an inner spherical node of radius ~200 μm, which is reasonable since 1) the optical penetration depth is ~1 μm and 2) the observed ablation depths for nominal energies are less than 100 μm. Importantly, these assumptions are not generally valid for most other laser sources.

Our simple model faithfully generates qualitative and, to a lesser extent, quantitative agreement with experimental observations. We measure and calculate a prompt rise in tissue temperature in the vicinity of the laser probe following irradiation (Figs. 3, 5, 7). Further, the model predicts a rapid decay of the temperature gradient in both the temporal and spatial domains; the temperature rise is small at distances greater than 1 mm from the energy source, and the thermal energy is dissipated promptly following cessation of irradiation (Figs. 3, 7).

The model is useful for understanding the influence of tissue properties on thermal transients (Figs. 8, 9) and for corroborationg and interpreting experimental data. For example, our model predicts that the temperature rise near the laser source will be greater in a medium with lower thermal conductivity (Figs. 8, 9). This result is intuitive since a lower thermal conductivity effectively reduces the volume available for storage of thermal energy; however, our model quantitatively calculates this effect. As vitreoretinal maneuvers are explored in saline, under air, and in vitreous substitutes such as perfluoro-N-octane (where the thermal properties are not well characterized, Infinitech, Inc., St. Louis, MO, personal communication), quantitative predictions of material thermal response are useful in the setting of altered thermophysical parameters.

Similarities are noted to the data of Mainster [26] who modeled the temperature rise in vitreous following carbon dioxide laser application. Spatial and temporal thermal gradients were calculated, but since the water absorption coefficient for CO_2 laser radiation (10.6 μm) is an order of magnitude less than that for erbium, considerably more energy must be applied to initiate photovaporization. Further, the optical penetration depth is an order of magnitude greater for carbon dioxide, resulting in less localized thermal effects. Following 220 mW application of 10.6 μm CO_2 laser output for 5 s, a temperature rise of ~75°C and ~25°C is calculated at distances 0.5 and 1.0 mm from the energy source, respectively [26].

Mainster [26] solves the heat conduction equation with analytical techniques, using numerical methods for approximation of the analytical solutions which are expressed as a function of integrals. An advantage of this technique is its suitability for solution using simple technology such as a programmable calculator. In contrast, we solve the heat conduction equation through iterative application of Fourier's law. This requires computer methods, but allows for greater flexibility in considering alternate pulse shape, repetition rate, boundary conditions, and sample geometry. These complexities have not been considered in the present study, but are readily approached with straightforward extensions of the method described above.

Discrepancies between the experimental and modeling data may reflect inaccurate estimation of vitreous thermophysical properties. Further, very fast mechanical processes may alter the geometry of energy deposition. Specifically, bubble formation may lead to non-conductive heat transfer and may allow for deeper tissue penetration of

laser energy [27]. Although multiple complexities have been excluded, our model reproduces many of the thermal transient phenomena observed experimentally.

Importantly, our experimental results in vitreous and our modeling studies suggest that there is rapid decay in the temperature profile in the temporal and spatial domains; there is rapid fall-off in temperature rise at distances greater than 1 mm from the point of application, and the temperature decays promptly after stopping laser application. Since tissue injury depends on the temperature rise integrated over the time, our results support the notion that *thermal* injury to adjacent ocular structures should be limited during short, intravitreal application of Er:YAG laser energy. Alternately, acoustomechanical effects associated with explosive vaporization of tissue water are potentially damaging; however, the precise micromechanical tissue interactions have not been rigorously explored, and further investigation in this area is warranted.

ACKNOWLEDGMENTS

This work was supported in part by Coherent, Inc. The Massachusetts Eye and Ear Infirmary has a proprietary interest in this technology by agreement with Coherent, Inc.

REFERENCES

1. Peyman GA, Katoh N. Effects of erbium:YAG laser on ocular structures. Int Ophthalmol 1987; 10:245–253.
2. Tsubota K. Application of erbium:YAG laser in ocular ablation. Ophthalmologica 1990; 200:117–122.
3. Ren Q, Venugopalan V, Schomacker K, Deutsch TF, Flotte TJ, Puliafito CA, Birngruber R. Mid-infrared laser ablation of cornea: a comparative study. Lasers Med Surg 1992; 12:274–281.
4. Gailitis RP, Patterson SW, Samuels MA, Hagen K, Ren Q, Waring GO. Comparison of laser phacovaporization using the Er:YAG and Er:YSGG laser. Arch Ophthalmol 1993; 111:697–700.
5. Bende T, Jean B, Matallana M, Seiler T. Thermal transients in the cornea during photoablation with the Er: YAG laser. Lasers Light Ophthalmol 1992; 5:79–82.
6. Margolis TI, Farnath DA, Destro M, Puliafito CA. Erbium:YAG laser surgery on experimental vitreous membranes. Arch Ophthalmol 1989; 107:424–428.
7. D'Amico DJ, Moulton RS, Theodossiadis PG, Yarborough JM. Erbium:YAG laser photothermal retinal ablation in enucleated rabbit eyes. Am J Ophthalmol 1994; 117:783–790.
8. Berger JW, Talamo JH, Kim SH, LaMarche KJ, D'Amico DJ, Synder RW, Marcellino G. Temperature measurements during phacoemulsification and Er:YAG laser phacoablation in model systems. J Cataract Refract Surg 1996; 22:372–378.
9. Berger JW, LaMarche KJ, Kim SH, D'Amico DJ, Talamo JH. Er:YAG laser drilling of cataractous lens: Predicting the ablation rate with a simple model. Proc SPIE 1995; 2393:148–159.
10. Snyder RW, Noecker RJ, Jones H. In vitro comparison of phacoemulsification and the erbium:YAG laser in lens capsule rupture. ARVO abstracts. Invest Ophthalmol Vis Sci [Suppl] 1994; 35:1934.
11. Noecker RJ, Kramer TR, Ellsworth LG, Yarborough JM, Snyder RW. Endolenticular phacolysis using erbium: YAG lasers on human autopsy lenses. ARVO abstracts. Invest Ophthalmol Vis Sci [Suppl] 1993; 34:1453.
12. Brazitikos PD, D'Amico DJ, Bernal MT, Walsh AW. Erbium:YAG laser surgery of the vitreous and retina. Ophthalmology 1995; 102:278–290.
13. Miller JB, Smith MR, Pincus F, Stockert M. Intraocular carbon dioxide laser photocautery. I. Animal experimentation. Arch Ophthalmol 1979; 97:2157–2162.
14. Miller JB, Smith MR, Boyer DS. Intraocular carbon dioxide laser photocautery. Indications and contraindications at vitrectomy. Ophthalmology 1980; 87:1112–1120.
15. Karlin DK, Jakobiec, FA, Harrison W, Bridges T, Patel CK, Stnad AR, Wood O. Endophotocoagulation in vitrectomy with a carbon dioxide laser. Am J Ophthalmol 1986; 101:445–450.
16. Meyers SM, Bonner RF, Rodrigues MM, Ballintine EJ. Phototransection of vitreal membranes with the carbon dioxide laser in rabbits. Ophthalmology 1983; 90:563–568.
17. Bochow TW, Kim RY, Berger JW, D'Amico DJ. Photovitrectomy—a novel approach for vitreous removal. ARVO abstracts. Invest Ophthalmol Vis Sci 1995; 36:S384.
18. Berger JW, Bochow TW, Kim RY, D'Amico DJ. Biophysical considerations for optimizing energy delivery during Er:YAG laser vitreoretinal surgery. Proc SPIE 1996; 2673:146–156.
19. Lagendijk JJW. A mathematical model to calculate temperature distributions in human and rabbit eyes during hyperthermic treatment. Phys Med Biol 1982; 27:1301–1311.
20. Shitzer A, Eberhart RC. Review of elementary heat transfer. In: Shitzer A, Eberhart RC eds. "Heat Transfer in Medicine and Biology," Volume 1. New York: Plenum Press. 1985, pp 411–418.
21. Waddell DE, Rylander G, Ghaffari S, Diller KR, Farrar RM. Transient temperature field in the eye during microwave irradiation at 35 GHz. Adv Biol Heat Mass Transfer 1992; 231:1–6.
22. Bowman HF, Cravalho EG, Woods M. Theory, measurement and application of thermal properties of biomaterials. Annu Rev Biophys Bioeng 1975; 4:43–80.
23. Chato JC. Selected thermophysical properties of biological materials. In: Shitzer A, Eberhart RC, eds. "Heat Transfer in Medicine and Biology," Volume 1. New York: Plenum Press. 1985, pp 413–418.
24. Borirakchanyavat S, Puliafito CA, Kliman GH, Margolis TI, Galler E. Holmium-YAG laser surgery on experimental vitreous membranes. Arch Ophthalmol 1991; 109: 1605–1609.
25. Mainster MA, White TJ, Tips JH, Wilson PW. Transient thermal behavior in biological systems. Bull Math Biophys 1970; 32:303–314.

26. Mainster MA. Ophthalmic applications of infrared lasers-thermal considerations. Invest Ophthalmol Vis Sci 1979; 18:414–420.

27. Lin CP, Stern D, Puliafito CA. High speed photography of Er:YAG laser ablation in fluid. Invest Ophthalmol Vis Sci 1990; 31:2546–2550.